

# In vivo viscoelastic properties of the brain in normal pressure hydrocephalus

Kaspar-Josche Streitberger<sup>a,†</sup>, Edzard Wiener<sup>b,†</sup>, Jan Hoffmann<sup>c,d</sup>, Florian Baptist Freimann<sup>e</sup>, Dieter Klatt<sup>a</sup>, Jürgen Braun<sup>f</sup>, Kui Lin<sup>g</sup>, Joyce McLaughlin<sup>g</sup>, Christian Sprung<sup>e</sup>, Randolph Klingebiel<sup>b,h,\*</sup> and Ingolf Sack<sup>a,\*\*</sup>

Nearly half a century after the first report of normal pressure hydrocephalus (NPH), the pathophysiological cause of the disease still remains unclear. Several theories about the cause and development of NPH emphasize disease-related alterations of the mechanical properties of the brain. MR elastography (MRE) uniquely allows the measurement of viscoelastic constants of the living brain without intervention. In this study, 20 patients (mean age, 69.1 years; nine men, 11 women) with idiopathic ( $n = 15$ ) and secondary ( $n = 5$ ) NPH were examined by cerebral multifrequency MRE and compared with 25 healthy volunteers (mean age, 62.1 years; 10 men, 15 women). Viscoelastic constants related to the stiffness ( $\mu$ ) and micromechanical connectivity ( $\alpha$ ) of brain tissue were derived from the dynamics of storage and loss moduli within the experimentally achieved frequency range of 25–62.5 Hz. In patients with NPH, both storage and loss moduli decreased, corresponding to a softening of brain tissue of about 20% compared with healthy volunteers ( $p < 0.001$ ). This loss of rigidity was accompanied by a decreasing  $\alpha$  parameter (9%,  $p < 0.001$ ), indicating an alteration in the microstructural connectivity of brain tissue during NPH. This disease-related decrease in viscoelastic constants was even more pronounced in the periventricular region of the brain. The results demonstrate distinct tissue degradation associated with NPH. Further studies are required to investigate the source of mechanical tissue damage as a potential cause of NPH-related ventricular expansions and clinical symptoms. Copyright © 2010 John Wiley & Sons, Ltd.

**Keywords:** MR elastography; brain; viscoelasticity; springpot; normal pressure hydrocephalus

## INTRODUCTION

Normal pressure hydrocephalus (NPH) was first observed and described in 1965 by Hakim and Adams (1), and represents an epidemiologically important disease with an incidence of 5.5 per 100,000 and a prevalence of 21.9 per 100,000 (2). The syndrome is

characterized by a triad of clinical symptoms: a slowly progressive gait disorder (usually the earliest feature of the syndrome), followed by symptomatic dementia and urinary incontinence. Cerebral imaging typically shows an enlargement of all ventricles, without sulcal widening, whereas cerebrospinal fluid (CSF)

\* Correspondence to: R. Klingebiel, Neuroradiology and Radiology Institute, Klinik im Park, Seestrasse 220, CH-8027 Zürich, Switzerland.  
E-mail: randolf.klingebiel@hirslanden.ch

\*\* Correspondence to: I. Sack, Department of Radiology, Charité – Universitätsmedizin Berlin, Charitéplatz 1, 10117 Berlin, Germany.  
E-mail: ingolf.sack@charite.de

a K.-J. Streitberger, D. Klatt, I. Sack  
Department of Radiology, Charité – University of Medicine Berlin, Berlin, Germany

b E. Wiener  
Department of Neuroradiology, Charité – University of Medicine Berlin, Berlin, Germany

c J. Hoffmann  
Department of Neurology, Charité – University of Medicine Berlin, Berlin, Germany

d J. Hoffmann  
Department of Neurology, University of California San Francisco, San Francisco, CA, USA

e F. B. Freimann, C. Sprung  
Neurosurgical Department, Charité – University of Berlin, Berlin, Germany

f J. Braun  
Institute of Medical Informatics, Charité – University of Medicine Berlin, Berlin, Germany

g K. Lin, J. McLaughlin  
Mathematics Department, Rensselaer Polytechnic Institute, Troy, NY, USA

h K. Lin, J. McLaughlin  
Neuroradiology and Radiology Institute, Klinik im Park, Zürich, Switzerland

† These authors contributed equally to this work.

**Abbreviations used:** CSF, cerebrospinal fluid;  $f$ ,  $\omega$ , driving (vibration) frequency, angular driving frequency;  $G^*$ ,  $G'$ ,  $G''$ ,  $\overline{G^*}$ ,  $\overline{G'}$ ,  $\overline{G''}$ , complex modulus, storage modulus, loss modulus and their spatially averaged quantities denoted by an overbar;  $\overline{G'}$ ,  $\overline{\alpha}$ , storage modulus and springpot power exponent, averaged over the drive frequency; MEG, motion encoding gradient; MRE, MR elastography; MS, multiple sclerosis; NPH, normal pressure hydrocephalus; PV, periventricular; ROI, region of interest; SD, standard deviation;  $\mathbf{x}$ , position vector;  $\overline{\mu}$ ,  $\overline{\alpha}$ , spatially averaged viscoelastic parameters according to the springpot model;  $\overline{\mu}$ ,  $\overline{\eta}$ , spatial averages of shear elasticity and shear viscosity derived by the springpot model.

pressure measurements usually remain within the normal range. Although these findings seem to be the result of an impaired CSF dynamic, the pathophysiological cause of these findings has not been clarified in detail. At present, the most widely accepted hypothesis is that transient intracranial pressure peaks lead to chronic mechanical stress on ventricular walls, finally resulting in ventricular dilatation and clinical impairment. Despite normal CSF pressures, the drainage of large amounts of CSF (50 mL as a tap test or prolonged CSF drainage via a spinal catheter) leads to a transient improvement in the clinical symptoms. However, the drainage of CSF by spinal tap or even by shunt operations, resulting in a reduction in the CSF pressure and improvement in the clinical symptoms, is not necessarily accompanied by recovery or a reduction in ventricular size (3). To date, the underlying mechanism that transmits relatively small CSF pressure peaks into a significant, irreversible ventricular enlargement remains obscure. Several mechanisms have been postulated, such as pressure differences between the ventricles and the subarachnoid space of the cerebral convexity, abnormalities of the periventricular (PV) brain parenchyma (4) and diminished vascular compliance (5–10). In addition to the mechanical component of NPH, metabolic and hemodynamic alterations in the brain parenchyma could also cause degradation of PV white matter (11). Considering the current theories of NPH, altered mechanical tissue properties seem to play an important role in its pathogenesis.

By combining MRI and shear waves, researchers are now in the position to measure the bulk mechanical properties of the living brain noninvasively (12–21). The reproducibility of MR elastography (MRE) of the brain has been addressed in several studies, indicating an excellent agreement of repeated measurements of viscoelastic parameters (15), as well as the consistency of these constants in healthy volunteers (22). Recently, an enhanced MRE technique has been introduced that utilizes multifrequency vibrations in order to acquire the dispersion function of the complex modulus (22).

The complex shear modulus is a widely used quantity measured in rheology and material sciences for the characterization of macromolecular networks by the strength and number of intranetwork connections (23). We use the terminology of the theory of viscoelasticity to derive two phenomenological constants that provide information about the shear elasticity of the tissue under investigation and its micromechanical arrangement. Both parameters, denoted  $\mu$  and  $\alpha$ , can be derived by the so-called 'springpot model', which is an interpolation between elastic spring and dashpot elements. Former studies of cerebral multifrequency MRE in volunteers and in patients with multiple sclerosis have employed this two-parameter model as a robust means to analyze the dispersion of the complex modulus and to draw conclusions about the micromechanical constitution of tissue (20,21). Our analysis is performed in multiple transverse

slices of the brain, where we compute 'global' moduli, i.e. their spatial average within the entire parenchyma visible in MR images. In addition, the average of  $\mu$  and  $\alpha$  in a smaller region is addressed by considering a region in the vicinity of the ventricular system. The results are compared with MRE data of liver, brain and muscle published in the literature, which have been analyzed by a similar viscoelastic model to that used herein.

## METHODS

Twenty patients with idiopathic ( $n = 15$ ) and secondary ( $n = 5$ ) NPH were included in the study [mean age, 69.1 years; standard deviation (SD), 8.1 years; nine men, 11 women]. The diagnosis of NPH was established according to the following criteria: (i) personal history and clinical evidence of the NPH triad (gait disturbance, cognitive impairment and incontinence); (ii) a lumbar puncture showing a normal or only slightly elevated CSF pressure ( $< 20 \text{ cmH}_2\text{O}$ ); and (iii) a clear improvement of the clinical impairment after a tap test of 50 mL or prolonged CSF drainage. Nonambulatory patients with a history of significant head injury, intracranial hemorrhage, meningitis or noncompliant severe dementia were excluded. Twenty-five healthy volunteers were recruited by advertisement (mean age, 62.1 years; SD, 7.0 years; 10 men, 15 women). They had no family history of dementia or personal history of any psychiatric or neurological disease, severe head trauma, any metabolic or endocrine disturbances, cancer, severe hypertension, heart disease, or alcohol or drug abuse, and did not demonstrate an increase in ventricular size. The study was approved by the local ethics committee (protocol No EA1/186/08). A description of the group statistics is given in Table 1.

### Cerebral MRE and data evaluation

Measurements were performed on a standard 1.5-T clinical MRI scanner (Sonata, Siemens, Erlangen, Germany). Mechanical vibrations were induced into the head by a custom-made head cradle connected via a carbon-fiber piston to a remote vibration generator as described in ref. (15). The vibration waveform was synthesized by a superposition of four harmonic oscillations of 25, 37.5, 50 and 62.5 Hz with equal phases and a total duration of 400 ms (22). A single burst of this signal was fed into the wave generator prior to the start of each image acquisition. Wave images were acquired using a spin-echo echo planar imaging sequence, which was sensitized to motion by a sinusoidal motion-encoding gradient (MEG) during the first half of the echo period. The center frequency of MEG was 60 Hz, with a length of MEG of four periods equal to 66.67 ms and an amplitude of 35 mT/m in the through-plane direction. The polarity of MEG was toggled in each second experiment to subtract the inverse phase contrast and leave the difference wave phase in the image. The

**Table 1.** Group description, mean age and age range; values in parentheses denote the standard deviation (SD)

	Healthy	NPH	Healthy male	NPH male	Healthy female	NPH female
<i>n</i>	25	20	10	9	15	11
Mean age (years)	62.1 (7.0)	69.1 (8.1)	63.8 (6.4)	69.1 (8.6)	60.9 (7.4)	69.0 (8.1)
Range (years)	51–72	51–78	51–72	51–78	51–72	53–78

NPH, normal pressure hydrocephalus.

experiment was repeated in order to capture the dynamics of wave propagation. Therefore, the delay between the onset of vibration and the start of motion encoding was varied 32 times from 320.0 to 397.5 ms by an increment of 2.5 ms. The resulting phase shift corresponds to a first harmonic frequency of 12.5 Hz which determines the resolution in our vibration spectrum. One dynamic scan (32 phase shifts acquired twice with alternating sign of MEG) was run per image slice. Three adjacent image planes with a slice thickness of 6 mm were selected in a central part through the ventricles parallel to the internal base of the skull. Of note, the resulting position of image slices with a central ventricular location was substantially different from the slice selection used in previous studies (15,20,21). Further image

acquisition parameters were as follows: TR = 3 s; TE = 149 ms; field of view, 192 × 192 mm; matrix size, 128 × 128. For data analysis, the time traces of the waves at each planar spatial point were Fourier transformed to create the time harmonic, complex, out-of-image plane displacement  $u(\mathbf{x}, f)$  at each of the mechanical driving frequencies  $f$  of 25, 37.5, 50 and 62.5 Hz. Figure 1a, b shows, in the top row, wave images (real parts of complex waves) at the four driving frequencies of a healthy volunteer and a patient.

Brain biomechanics comparisons are reported based on the complex shear modulus  $G^*(x, f)$  in the parenchyma excluding the ventricles. Using a locally constant assumption for the complex modulus  $G^*(x, f)$ , the relationship  $G^*(x, f) = -(2\pi f)^2 \rho u(x, f) / \Delta u(x, f)$ ,

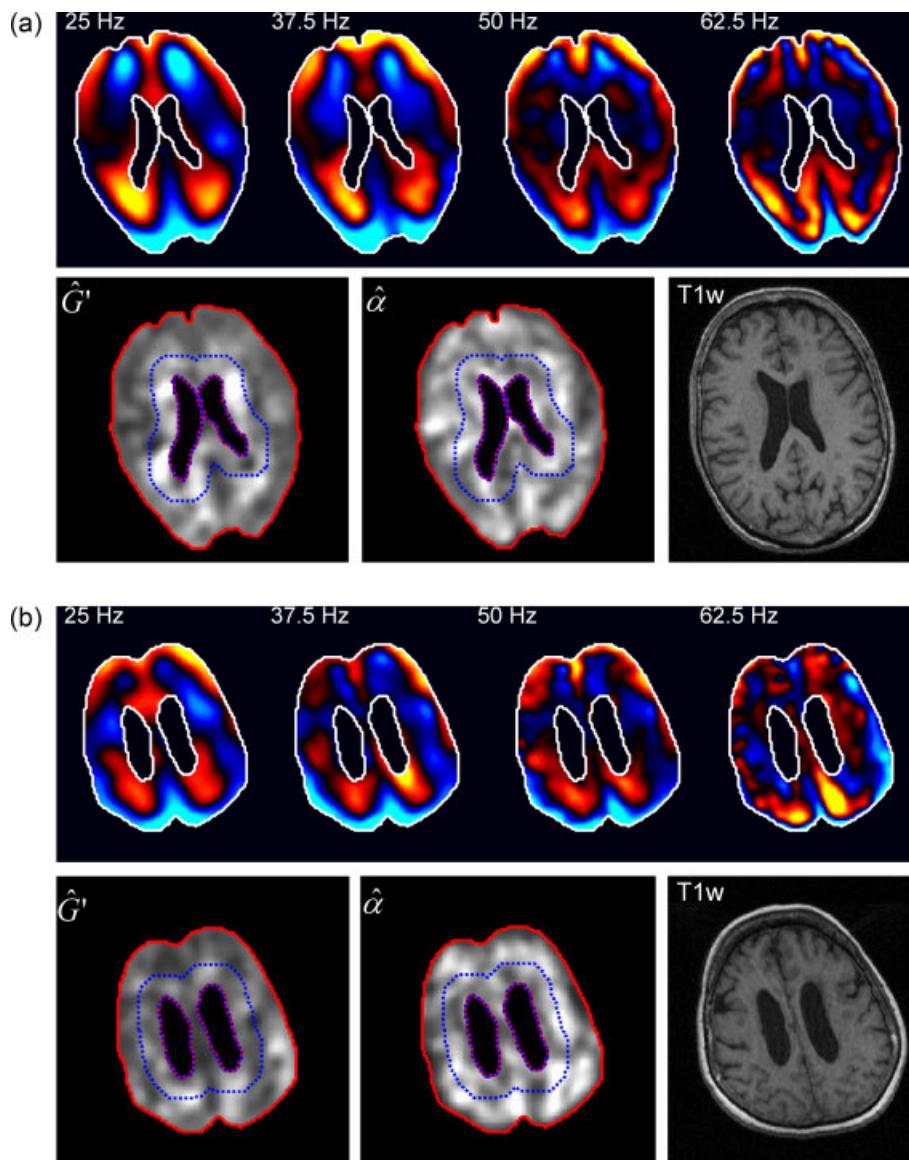


**Figure 1.** Top row: wave images after Fourier decomposition (real part). The vibration frequency is given in the top left-hand corner. Blue color scales vibrations towards the reader, and red to yellow color scales motion beneath the image plane. The maximum tissue deflection is approximately 80  $\mu\text{m}$ . Bottom row: spatially resolved constitutive parameters  $\hat{G}(x)$  and  $\hat{\alpha}(x)$  according to the springpot model. The images were calculated from four complex modulus images corresponding to the four experimentally applied driving frequencies. Further details are given in 'Methods'. Red lines demarcate the region of interest used for averaging global moduli; blue/dotted lines show the region used for the quantification of periventricular  $\bar{\mu}$  and  $\bar{\alpha}$  values.  $\hat{G}$  and  $\hat{\alpha}$  images are linearly scaled from 0 to 3.0 kPa and from 0 to 0.6, respectively. The  $T_1$ -weighted image (T1w) shows anatomical details. (a) Healthy volunteer (female, 72 years); (b) patient with normal pressure hydrocephalus (NPH) (female, 70 years).

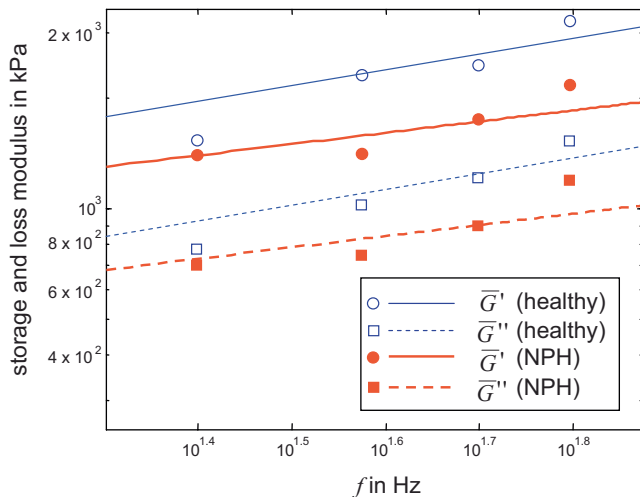


**Figure 2.** Dispersion data from the global complex modulus acquired in a patient with normal pressure hydrocephalus (NPH) (female, 70 years; red symbols) and a healthy volunteer (female, 72 years; blue symbols). The data show the global complex moduli, averaged within the entire parenchyma of the image slices (cf. Fig. 1). The fitted curves (line graphs) were calculated by the viscoelastic springpot model that incorporates two variables  $\bar{\kappa}$  and  $\bar{\alpha}$ . Thus, only two parameters were needed to fit eight data points (four  $\bar{G}'$  and four  $\bar{G}''$  moduli). The slope of the lines is given by  $\bar{\alpha}$ , which is significantly lower in patients with NPH compared with healthy volunteers.

where  $\rho = 1000 \text{ kg/m}^3$  is the tissue density within the brain parenchyma, was used to calculate  $G^*(x, f)$  in all image planes at each frequency. The global  $\bar{G}^*(f)$  was calculated by averaging  $G^*(x, f)$  over all parenchyma spatial points in all planes. The springpot model for  $\bar{G}^*(f) = \bar{\kappa}(2\pi f i)^{\bar{\alpha}}$ , where  $\bar{\kappa} = \bar{\mu}^{1-\bar{\alpha}} \bar{\eta}^{\bar{\alpha}}$ , and  $\bar{\kappa}$ ,  $\bar{\alpha}$  are frequency independent. The parameter  $\bar{\mu}$  is the global shear elasticity,  $\bar{\eta}$  is the viscous damping and  $\bar{\alpha}$  is a measure of the elastic lossy relation. For example,  $\bar{\alpha} = 0$  corresponds to lossless elastic behavior with shear elasticity  $\bar{\mu}$ , and  $\bar{\alpha} = 1$  to lossy viscous damping with viscosity  $\bar{\eta}$ . It should be noted that, when considering spatially averaged quantities, the springpot model will yield a linear dependence on  $\log f$  with slope  $\bar{\alpha}$  when  $\bar{G}^*(f)$  is displayed on a logarithmic scale (see Fig. 2).

The global storage modulus  $\bar{G}'(f) = \text{Re}\bar{G}^*(f)$  and global loss modulus  $\bar{G}''(f) = \text{Im}\bar{G}^*(f)$  are given in Table 2. The parameters  $\bar{\kappa}$  and  $\bar{\alpha}$  were determined by a least-squares fit over the frequency of the tabulated global  $\bar{G}^*(f)$  using the springpot model. We present values of  $\bar{G}'(f)$ ,  $\bar{G}''(f)$ ,  $\bar{\alpha}$  and  $\bar{\mu}$  where, for the latter parameter, we assume  $\bar{\eta} = 3.7 \text{ Pa}$ . This value of  $\bar{\eta}$  was previously determined as an approximated value of viscosity in human brain tissue (20). As there are no other frequency-independent viscosity values of *in vivo* human brain in the literature, we propose this value for translating  $\bar{\kappa}$  to elasticity. This scaling of  $\bar{\kappa}$  from a dimension ( $\text{Pa s}^\alpha$ ) that depends on  $\alpha$  to an elasticity improves the comparability of multifrequency MRE results with other elastography studies without changing the significance of the determined mechanical constants.

For demonstration purposes,  $\hat{G}'(x)$ , which is  $G'(x, f)$  averaged over all four driving frequencies, and  $\hat{\alpha}(x)$  images are shown in Fig. 1a, b (bottom rows). The  $\hat{\alpha}$  images were calculated by averaging over the driving frequencies, that is averaging over the springpot-inherent relation for  $\alpha$ ,  $2/\pi \arctan[G''(x, f)/G'(x, f)]$ . In Fig. 1, the considered regions of interest (ROIs) are drawn. The

main ROI is the entire parenchyma, but we also consider the PV ROI outlined in the bottom rows, where these outlines are superimposed on the grayscale images of  $\hat{G}'(x)$  and  $\hat{\alpha}(x)$ . The main conclusions are drawn from the 'global' moduli  $\bar{G}'(f)$ ,  $\bar{G}''(f)$ , which are determined from the entire brain parenchyma visible in the image slice. In addition, the PV subregion was derived by an automatic dilatation of the ventricle boundary towards a 10-pixel-wide ring. When this ring extended outside the whole brain image, only points within the brain were used. Although, in general, this 10-pixel-wide ring contained less than the whole brain image, it is still a substantial subregion of the brain. In future studies, we will consider rings of varying size to determine possible ring radius elasticity properties. Henceforth, we refer to the 10-pixel-wide ring around the boundary of the ventricles as the 'PV' ROI. The frequency-independent constitutive parameters  $\bar{\mu}$  and  $\bar{\alpha}$  are tabulated for this PV subregion.

### Statistical data analysis

Four storage moduli  $\bar{G}'$ , four loss moduli  $\bar{G}''$  and two constitutive parameters  $\bar{\mu}$  and  $\bar{\alpha}$  were analyzed for each participant. All data were distributed approximately normally, which was revealed by a Shapiro–Wilk parametric hypothesis test of composite normality. Statistical hypotheses were tested by a two-sided Student's *t*-test. The level of significance was 0.05. For statistical analysis, the Matlab R2007b statistics toolbox (The MathWorks Inc., Natick, MA, USA) was used.

## RESULTS

Figure 3 shows a significant decrease in cerebral viscoelasticity, given by a reduction in  $\bar{\mu}$  and  $\bar{\alpha}$ , in patients with NPH compared with healthy volunteers. The shear elasticity  $\bar{\mu}$  decreased by about 0.57 kPa (−20%) from 2.84 to 2.27 kPa. The connectivity parameter  $\bar{\alpha}$  decreased by about 0.025 (−9%) from 0.287 to 0.262 (see Table 2) ( $p < 0.01$ ). Similar findings were encountered in men and women, with relative changes in  $\bar{\mu}$  of −20% in both groups. The connectivity parameter  $\bar{\alpha}$  was found to decrease by 7% in men and 9% in women.

All measured complex moduli were decreased significantly in patients by both real and imaginary parts. This change in  $\bar{G}^*$  dispersion is illustrated in Fig. 2. In addition, a decrease in both slopes of  $\bar{G}'(f)$  and  $\bar{G}''(f)$  is perceptible, corresponding to a lower  $\bar{\alpha}$  value in patients. A symptomatic decrease in  $\hat{G}'(x)$  and  $\hat{\alpha}(x)$  is further demonstrated in Fig. 1, where  $\hat{G}'(x)$  and  $\hat{\alpha}(x)$  maps appear darker in diseased brain, particularly near the ventricles.

Table 2 summarizes the relevant viscoelastic data of this study. It is shown that the global parenchyma ROIs of patients are smaller ( $117 \pm 19 \text{ cm}^2$ ) than in healthy volunteers ( $152 \pm 14 \text{ cm}^2$ ) because of the enlarged ventricles. However, this effect is reversed when accounting for PV ROIs, with a mean size of  $48 \pm 12 \text{ cm}^2$  in patients and  $37 \pm 7 \text{ cm}^2$  in volunteers. Of note, irrespective of these differences in ROI size, the decrease in  $\bar{\mu}$  and  $\bar{\alpha}$  is significant in both regions, and even enhanced in the vicinity of the ventricular system.

## DISCUSSION

Although representing an epidemiologically important disease, NPH and its underlying pathophysiology are still poorly understood and subject to controversial discussions (24). Different

**Table 2.** Viscoelastic parameters  $\bar{\mu}$  and  $\bar{\alpha}$  according to the springpot model.  $\bar{G}$  and  $\bar{G}''$  denote the frequency-dependent storage and loss moduli, respectively.  $\Delta$  refers to the difference between the groups [normal pressure hydrocephalus (NPH) vs healthy volunteers]. In addition, the size of the considered region of interest (ROI) is given, with 'PV' denoting the periventricular region. Values in parentheses correspond to standard deviations. Viscoelastic parameters are given in kPa, except for dimensionless  $\bar{\alpha}$ .

	All subjects		Males		Females	
	NPH	Controls	NPH	Controls	NPH	Controls
$\bar{\mu}$	2.27 (0.24)	2.84 (0.44)	2.20 (0.27)	2.76 (0.54)	2.32 (0.21)	2.90 (0.36)
$\Delta$	-0.57 kPa		-0.56 kPa		-0.58 kPa	
	-25.1%		-20.3%		-20.0%	
	$p < 0.001$		$p < 0.05$		$p < 0.001$	
$\bar{\alpha}$	0.262 (0.011)	0.287 (0.011)	0.265 (0.011)	0.286 (0.013)	0.260 (0.010)	0.287 (0.011)
$\Delta$	-0.025		-0.021		-0.027	
	-9.5%		-7.3%		-9.4%	
	$p < 0.001$		$p < 0.01$		$p < 0.001$	
$\bar{G}$ (25Hz)	1.34 (0.15)	1.50 (0.13)	1.27 (0.14)	1.46 (0.16)	1.39 (0.13)	1.52 (0.11)
$\Delta$	-0.16 kPa		-0.19 kPa		-0.13 kPa	
	-11.9%		-13.0%		-8.6%	
	$p < 0.001$		$p < 0.05$		$p < 0.01$	
$\bar{G}$ (37.5Hz)	1.60 (0.14)	1.82 (0.21)	1.53 (0.11)	1.77 (0.23)	1.66 (0.14)	1.85 (0.19)
$\Delta$	-0.22 kPa		-0.24 kPa		-0.19 kPa	
	-13.8%		-13.6%		-10.3%	
	$p < 0.001$		$p < 0.01$		$p < 0.05$	
$\bar{G}$ (50Hz)	1.76 (0.15)	1.94 (0.23)	1.73 (0.17)	1.91 (0.30)	1.78 (0.13)	1.97 (0.17)
$\Delta$	-0.18 kPa		-0.18 kPa		-0.19 kPa	
	-10.2%		-9.4%		-9.6%	
	$p < 0.001$		$p = 0.115$		$p < 0.05$	
$\bar{G}$ (62.5Hz)	2.19 (0.28)	2.38 (0.22)	2.15 (0.31)	2.33 (0.23)	2.22 (0.26)	2.42 (0.22)
$\Delta$	-0.19 kPa		-0.18 kPa		-0.2 kPa	
	-8.7%		-7.7%		-8.3%	
	$p < 0.05$		$p = 0.179$		$p = 0.056$	
$\bar{G}''$ (25Hz)	0.56 (0.09)	0.70 (0.10)	0.55 (0.11)	0.68 (0.10)	0.57 (0.08)	0.72 (0.10)
$\Delta$	-0.14 kPa		-0.13 kPa		-0.15 kPa	
	-25.0%		-19.1%		-20.8%	
	$p < 0.001$		$p < 0.05$		$p < 0.001$	
$\bar{G}''$ (37.5Hz)	0.65 (0.07)	0.84 (0.10)	0.63 (0.08)	0.83 (0.12)	0.66 (0.07)	0.84 (0.09)
$\Delta$	-0.19 kPa		-0.2 kPa		-0.18 kPa	
	-29.2%		-24.1%		-21.4%	
	$p < 0.001$		$p < 0.001$		$p < 0.001$	
$\bar{G}''$ (50Hz)	0.79 (0.07)	0.98 (0.15)	0.77 (0.07)	0.95 (0.19)	0.82 (0.07)	1.00 (0.13)
$\Delta$	-0.19 kPa		-0.18 kPa		-0.18 kPa	
	-24.1%		-18.9%		-18.0%	
	$p < 0.001$		$p < 0.05$		$p < 0.001$	
$\bar{G}''$ (62.5Hz)	1.03 (0.13)	1.20 (0.19)	1.01 (0.15)	1.18 (0.17)	1.05 (0.12)	1.22 (0.20)
$\Delta$	-0.17 kPa		-0.17 kPa		-0.17 kPa	
	-16.5%		-14.4%		-13.9%	
	$p < 0.01$		$p < 0.05$		$p < 0.05$	
ROI size (cm <sup>2</sup> )	117 (19)	152 (14)	119 (22)	160 (15)	116 (17)	146 (10)
$\Delta$	-35 cm <sup>2</sup>		-41 cm <sup>2</sup>		-30 cm <sup>2</sup>	
	-29.9%		-25.6%		-20.5%	
	$p < 0.001$		$p < 0.001$		$p < 0.001$	
$\bar{\mu}$ (PV)	2.83 (0.61)	4.03 (0.77)	2.89 (0.82)	3.83 (0.66)	2.78 (0.40)	4.16 (0.84)
$\Delta$	-1.2 kPa		-0.94 kPa		-1.38 kPa	
	-42.4%		-24.5%		-33.2%	
	$p < 0.001$		$p < 0.05$		$p < 0.001$	

(Continues)

**Table 2. (Continued)**

	All subjects		Males		Females	
	NPH	Controls	NPH	Controls	NPH	Controls
$\bar{\alpha}$ (PV)	0.292 (0.020)	0.321 (0.015)	0.299 (0.019)	0.323 (0.020)	0.286 (0.020)	0.320 (0.011)
$\Delta$	-0.029		-0.024		-0.034	
	-9.9%		-7.4%		-10.6%	
	$p < 0.001$		$p < 0.05$		$p < 0.001$	
ROI size (cm <sup>2</sup> ) (PV)	48 (12)	37 (7)	45 (16)	38 (8)	50 (8)	36 (7)
$\Delta$	+11 cm <sup>2</sup>		+7 cm <sup>2</sup>		+14 cm <sup>2</sup>	
	+22.9%		+18.4%		+38.9%	
	$p < 0.001$		$p = 0.263$		$p < 0.001$	

mechanisms have been suggested as possible causes of NPH, including impaired absorption of CSF, deep white matter abnormalities, redistribution of vascular pulsations and decreased compliance of the brain parenchyma, vessels and subarachnoid spaces (5–10). The neurological symptoms have been related to interstitial edema in PV white matter and changes in brain tissue perfusion. Several of these mechanisms are related to the complex shear modulus of the brain. Only recently has noninvasive imaging of the complex shear modulus in the brain been possible (17–21).

This study is the first to assess alterations in the viscoelastic properties of brain tissue in NPH. Our raw complex modulus data  $\bar{G}$  and  $\bar{G}'$  clearly show that NPH is associated with a decrease in elasticity, i.e. stiffness, and thus an increase in brain tissue compliance. In addition to stiffness, multifrequency MRE, combined with viscoelastic modeling, is able to reveal details about the micromechanical connectivity of biological tissue. To achieve this, we analyzed the springpot-inherent power law behavior of  $\bar{G}^*$ , which can be explained by generalized Gaussian structures built from hierarchically ordered networks of viscous beads and elastic springs (23). These fractal networks are of special interest, as the displacement in the micromechanical model is represented in terms of well-defined eigenvalues of the connectivity matrix, which, in turn, determine the macrodispersion relation (25). Depending on the size and connectivity of

fractal networks, their dynamics scale over several orders of magnitude and yield a fractional power of frequency dependence within the intermediate frequency range applied in our experiments (26). The property of this resultant scaling is seen in the springpot model, indicating that the functions  $\log(\bar{G})$  and  $\log(\bar{G}')$  are linear as functions on  $\log(f)$ , with a slope  $\bar{\alpha}$  and an offset  $\log[\bar{\kappa}(2\pi)^{\bar{\alpha}} \cos(\bar{\alpha}\pi/2)]$  and  $\log[\bar{\kappa}(2\pi)^{\bar{\alpha}} \sin(\bar{\alpha}\pi/2)]$ , respectively. As such, the two-parameter springpot model is the simplest two-parameter model that reproduces the experimentally observed linear increase in  $\bar{G}^*$  on a logarithmic scale, as demonstrated in Fig. 2. The Voigt and Maxwell body models are classical two-parameter models which are, however, incapable of reproducing the monotonic increase in  $\bar{G}'$  and  $\bar{G}''$  within the frequency range of our experiments (20,22). Adding an additional variable, as performed in the three-parameter Zener model, yields a better fit to individual modulus dispersion data (22), but without improving the significance of the revealed constants to brain physiology given by, for example, age and gender aspects (20). Furthermore, the higher degree of freedom of the model renders the interpretation of the determined constants rather cumbersome. The parameter  $\bar{\mu}$  deduced from the springpot model reveals an elastic softening of the brain in patients with NPH. The parameter  $\bar{\alpha}$  indicates a decreasing number of mechanical connections, and thus reveals an alteration of the micromechanical network topology in the

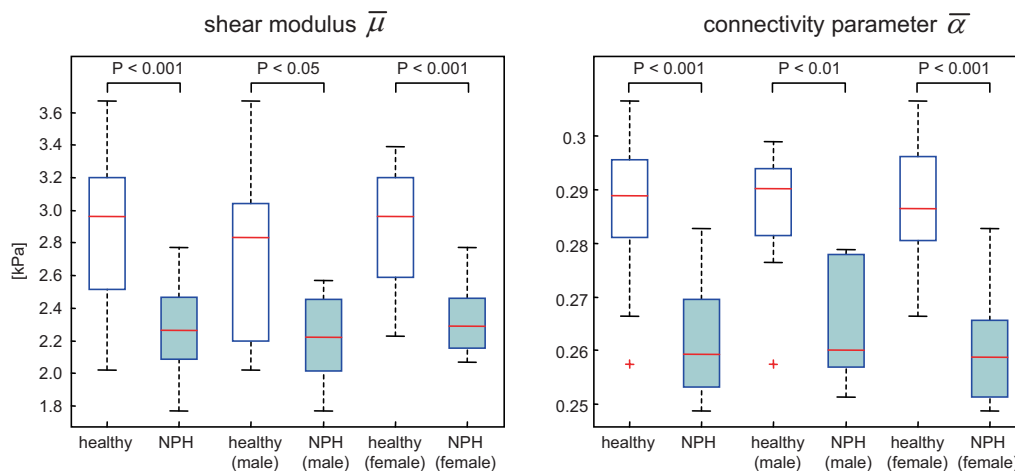


**Figure 3.** Patients with normal pressure hydrocephalus (NPH) present a global reduction in shear elasticity  $\bar{\mu}$  on the order of 20%. A similar loss of brain stiffness is seen in the subgroups of male and female patients. The connectivity parameter  $\bar{\alpha}$  is decreased in patients (–9%), corresponding to a reduction in wave energy loss and a transition of viscous brain tissue towards an elastic body.

diseased brain. In other words, relatively strong mechanical connections are replaced by fewer and relatively weak bonds. This scenario is seen in the degradation of both  $\bar{\mu}$  and  $\bar{\alpha}$ , implying the degradation of the micromechanical matrix of the brain in patients with NPH.

Modeling of *in vivo* viscoelastic data by the springpot model has been applied to several *in vivo* systems. These include liver for staging fibrosis (27,28), breast for the characterization of tumors (29), relaxed and contracted skeletal muscle (30) and brain affected by multiple sclerosis (MS) (21) and physiological aging (20). Among these systems,  $\bar{\mu}$  increased as a result of liver fibrosis, breast tumor malignancy and muscle contraction. Furthermore,  $\bar{\mu}$  decreased in normally aging brain by a rate of 15 Pa/year (20). Patients suffering from MS presented a decrease in  $\bar{\mu}$  of 273 Pa (−13%) compared with healthy controls (21). Thus, in NPH, we observed twice the effect of global brain softening relative to patients with MS. Considering the average age difference between patients and controls of 7 years in our study, the decrease in  $\bar{\mu}$  is still 1.7 times larger than that observed in patients with MS. In the literature,  $\bar{\alpha}$  was not influenced significantly by the progression of liver fibrosis (27,29) or neuronal degradation as a result of physiological aging (20). When  $\bar{\mu}$  changes and  $\bar{\alpha}$  does not, this indicates that the strength of the mechanical connections is altered, but their number and alignment are not. In contrast, in malignant breast tumors (31), as well as in contracted muscle (30),  $\bar{\alpha}$  increased significantly, which indicates the establishment of new mechanical bonds. The fact that we observed the reverse mechanism in NPH, i.e. a decrease in  $\bar{\mu}$  and  $\bar{\alpha}$ , may improve the understanding of the pathophysiological processes of this disease.

It is notable that the modulus values measured in this study are substantially larger than those determined by other two-dimensional MRE studies of the brain (21). We attribute this effect to a different slice positioning compared with previous studies. As mentioned in 'Methods', in the current study, transverse image slices were aligned through the centre of the lateral ventricles. In contrast, other studies (15,20,21) used slices in a more peripheral slab of the brain through the upper part or slightly above the ventricles. A higher proportion of sulci in that area might cause increased wave scattering, which certainly will influence the interpretation of wavelengths by inversion algorithms (32). Clearly, such effects of shear wave propagation through heterogeneous, porous, vascularized and anisotropic media need to be analyzed in further detail. In particular, the sensitivity of MRE to anisotropic viscoelastic constants of cerebral tissue, and their exploitation for addressing clinically relevant questions, remains an open field of research. In this respect, other quantitative MRI methods might support the analysis of MRE wave data by, for example, providing information about fiber alignment or tissue perfusion. One important structure-sensitive imaging method is diffusion MRI, which has revealed an increased water accumulation in PV tissue of patients with NPH via the alternative egress of CSF via extracellular spaces (33,34). Future studies should combine different quantitative MRI methods to assemble a more complete picture of the microstructural changes in cerebral tissue in NPH. MRE can contribute to this by showing that mechanical adhesion is reduced, corresponding to an increased possibility for CSF absorption. However, substantial research is required in order to derive valid microdriven macromechanostructural models that address the major remaining questions about the interaction of CSF drainage, interstitial water content, tissue porosity, tissue

matrix stiffness and clinical symptoms. Our results may contribute to the search for models capable of explaining the mechanisms of NPH.

## CONCLUSIONS

Multifrequency MRE reveals a substantial change in the viscoelastic properties of the brain in patients with NPH. A pronounced decrease in shear modulus and shear modulus dispersion slope was observed in tissue areas near the ventricular system. Further studies are required to translate these initial findings into a valid model of the mechanism of disease progression in NPH.

## Acknowledgements

This work was supported by the German Research Foundation (Sa/901-3) and the Centre for Stroke Research Berlin (BMBF 01 EO 0801).

## REFERENCES

- Hakim S, Adams RD. The special clinical problem of symptomatic hydrocephalus with normal cerebrospinal fluid pressure. Observations on cerebrospinal fluid hydrodynamics. *J. Neurol. Sci.* 1965; 2: 307–327.
- Shprecher D, Schwalb J, Kurlan R. Normal pressure hydrocephalus: diagnosis and treatment. *Curr. Neurol. Neurosci. Rep.* 2008; 8: 371–376.
- Sprung C, Miethke C, Schlosser HG, Brock M. The enigma of under-drainage in shunting with hydrostatic valves and possible solutions. *Acta Neurochir. Suppl.* 2005; 95: 229–235.
- Edwards RJ, Dombrowski SM, Luciano MG, Pople IK. Chronic hydrocephalus in adults. *Brain Pathol.* 2004; 14: 325–336.
- Greitz D. Radiological assessment of hydrocephalus: new theories and implications for therapy. *Neurosurg. Rev.* 2004; 27: 145–165; discussion 166–167.
- Bradley WG Jr, Whittemore AR, Watanabe AS, Davis SJ, Teresi LM, Homyak M. Association of deep white matter infarction with chronic communicating hydrocephalus: implications regarding the possible origin of normal-pressure hydrocephalus. *Am. J. Neuroradiol.* 1991; 12: 31–39.
- Egnor M, Zheng L, Rosiello A, Gutman F, Davis R. A model of pulsations in communicating hydrocephalus. *Pediatr. Neurosurg.* 2002; 36: 281–303.
- Bateman GA. Vascular compliance in normal pressure hydrocephalus. *Am. J. Neuroradiol.* 2000; 21: 1574–1585.
- Bateman GA. The pathophysiology of idiopathic normal pressure hydrocephalus: cerebral ischemia or altered venous hemodynamics? *Am. J. Neuroradiol.* 2008; 29: 198–203.
- Silverberg GD. Normal pressure hydrocephalus (NPH): ischaemia, CSF stagnation or both. *Brain* 2004; 127: 947–948.
- Kondziella D, Sonnewald U, Tullberg M, Wikkelsö C. Brain metabolism in adult chronic hydrocephalus. *J. Neurochem.* 2008; 106: 1515–1524.
- McCracken PJ, Manduca A, Felmlee J, Ehman RL. Mechanical transient-based magnetic resonance elastography. *Magn. Reson. Med.* 2005; 53: 628–639.
- Hamhaber U, Sack I, Papazoglou S, Rump J, Klatt D, Braun J. Three-dimensional analysis of shear wave propagation observed by *in vivo* magnetic resonance elastography of the brain. *Acta Biomater.* 2007; 3: 127–137.
- Xu L, Lin Y, Han JC, Xi ZN, Shen H, Gao PY. Magnetic resonance elastography of brain tumors: preliminary results. *Acta Radiol.* 2007; 48: 327–330.
- Sack I, Beierbach B, Hamhaber U, Klatt D, Braun J. Non-invasive measurement of brain viscoelasticity using magnetic resonance elastography. *NMR Biomed.* 2008; 21: 265–271.

16. Kruse SA, Rose GH, Glaser KJ, Manduca A, Felmlee JP, Jack CR Jr, Ehman RL. Magnetic resonance elastography of the brain. *Neuroimage* 2008; 39: 231–237.
17. Green MA, Bilston LE, Sinkus R. In vivo brain viscoelastic properties measured by magnetic resonance elastography. *NMR Biomed.* 2008; 21: 755–764.
18. Vappou J, Breton E, Choquet P, Willinger R, Constantinesco A. Assessment of in vivo and post-mortem mechanical behavior of brain tissue using magnetic resonance elastography. *J. Biomech.* 2008; 41: 2954–2959.
19. Atay SM, Kroenke CD, Sabet A, Bayly PV. Measurement of the dynamic shear modulus of mouse brain tissue in vivo by magnetic resonance elastography. *J. Biomech. Eng.* 2008; 130: 021013.
20. Sack I, Beierbach B, Wuerfel J, Klatt D, Hamhaber U, Papazoglou S, Martus P, Braun J. The impact of aging and gender on brain viscoelasticity. *Neuroimage* 2009; 46: 652–657.
21. Wuerfel J, Paul F, Beierbach B, Hamhaber U, Klatt D, Papazoglou S, Zipp F, Martus P, Braun J, Sack I. MR-elastography reveals degradation of tissue integrity in multiple sclerosis. *Neuroimage* 2010; 49: 2520–2525.
22. Klatt D, Hamhaber U, Asbach P, Braun J, Sack I. Noninvasive assessment of the rheological behavior of human internal organs using multifrequency MR elastography: a study of brain and liver viscoelasticity. *Phys. Med. Biol.* 2007; 52: 7281–7294.
23. Gurtovenko AA, Blumen A. Generalized Gaussian structures: models for polymer systems with complex topologies. In *Polymer Analysis, Polymer Theory*, Vol. 182, Advances in Polymer Science. Springer: Berlin, 2005; 171–282.
24. Bret P, Guyotat J, Chazal J. Is normal pressure hydrocephalus a valid concept in 2002? A reappraisal in five questions and proposal for a new designation of the syndrome as 'chronic hydrocephalus'. *J. Neurol. Neurosurg. Psychiatry* 2002; 73: 9–12.
25. Blumen A, Jurjiu A. Multifractal spectra and the relaxation of model polymer networks. *J. Chem. Phys.* 2002; 116: 2636–2641.
26. Jurjiu A, Friedrich C, Blumen A. Strange kinetics of polymeric networks modelled by finite fractals. *Chem. Phys.* 2002; 284: 221–231.
27. Klatt D, Asbach P, Somasundaram R, Hamm B, Braun J, Sack I. Assessment of the solid–liquid behavior of the liver for the diagnosis of diffuse disease using magnetic resonance elastography. *Rofo-Fortschr. Gebiet Rontgenstrahlen Bildgebenden Verfahren* 2008; 180: 1104–1109.
28. Asbach P, Klatt D, Schlosser B, Biermer M, Muche M, Rieger A, Loddenkemper C, Somasundaram R, Berg T, Hamm B, Braun J, Sack I. Viscoelasticity-based staging of hepatic fibrosis with multifrequency MR elastography. *Radiology* 2010; DOI: 10.1148/radiol.10092489.
29. Sinkus R, Tanter M, Siegmann K, Fink M. Breast cancer exhibits liquid-like mechanical properties – a comparative study between MR mammography and MR elastography. *Proceedings of the 15th Annual Meeting of ISMRM*, Berlin, Germany, 2007; 963.
30. Klatt D, Hamhaber U, Papazoglou S, Rettig K, Nuzha H, Braun J, Sack I. Multifrequency MR elastography on human thigh muscle in relaxation and in contraction. *Proceedings of the 17th Scientific Meeting of ISMRM*, Honolulu, HI, USA, 2009; 2499.
31. Sinkus R, Siegmann K, Xydeas T, Tanter M, Claussen C, Fink M. MR elastography of breast lesions: understanding the solid/liquid duality can improve the specificity of contrast-enhanced MR mammography. *Magn. Reson. Med.* 2007; 58: 1135–1144.
32. Papazoglou S, Xu C, Hamhaber U, Siebert E, Bohner G, Klingebiel R, Braun J, Sack I. Scatter-based magnetic resonance elastography. *Phys. Med. Biol.* 2009; 54: 2229–2241.
33. Bradley WG Jr, Bahl G, Alksne JF. Idiopathic normal pressure hydrocephalus may be a 'two hit' disease: benign external hydrocephalus in infancy followed by deep white matter ischemia in late adulthood. *J. Magn. Reson. Imaging* 2006; 24: 747–755.
34. Ng SE, Low AM, Tang KK, Chan YH, Kwok RK. Value of quantitative MRI biomarkers (Evans' index, aqueductal flow rate, and apparent diffusion coefficient) in idiopathic normal pressure hydrocephalus. *J. Magn. Reson. Imaging* 2009; 30: 708–715.